

# DeepMerge: Deep Learning-Based Region-Merging for Image Segmentation

Xianwei Lv<sup>a,b,\*</sup>, Claudio Persello<sup>b</sup>, Xiao Huang<sup>c</sup>, Dongping Ming<sup>d</sup>, Alfred Stein<sup>a</sup>

<sup>a</sup>*State Key Laboratory of Information Engineering in Surveying, Mapping and Remote Sensing, Wuhan University, Wuhan 430079, China*

<sup>b</sup>*Dept. of Earth Observation Science, Faculty ITC, University of Twente, 7500AE Enschede, the Netherlands*

<sup>c</sup>*The Department of Geosciences, University of Arkansas, Fayetteville, AR, USA*

<sup>d</sup>*School of Information Engineering, China University of Geosciences (Beijing), 29 Xueyuan Road, Haidian, Beijing 100083, China*

---

## Abstract

Accurate segmentation of large areas from very high spatial-resolution (VHR) remote sensing imagery remains a challenging issue in image analysis. Existing supervised and unsupervised methods both suffer from the large variance of object sizes and the difficulty in scale selection, which often result in poor segmentation accuracies. To address the above challenges, we propose a deep learning-based region-merging method (DeepMerge) to handle the segmentation in large VHR images by integrating a Transformer with a multi-level embedding module, a segment-based feature embedding module and a region-adjacency graph model. In addition, we propose a modified binary tree sampling method to generate multi-level inputs from initial segmentation results, serving as inputs for the DeepMerge model. To our best knowledge, the proposed method is the first to use deep learning to learn the similarity between adjacent segments for region-merging. The proposed DeepMerge method is validated using a remote sensing image of 0.55 m resolution covering an area of 5,660 km<sup>2</sup> acquired from Google Earth. The experimental results show that the proposed DeepMerge with the highest  $F$  value (0.9446) and the lowest  $TE$  (0.0962) and  $ED2$  (0.8989) is able to correctly segment objects of different sizes and outperforms all selected competing segmentation methods

---

\*Corresponding author. E-mail address: xianweilv@whu.edu.cn (Xianwei Lv)

from both quantitative and qualitative assessments.

*Keywords:* Image segmentation, Region-merging, Deep learning, Transformers, Remote sensing

---

## 1. Introduction

Acquiring very high-spatial-resolution (VHR) remote sensing images over large areas has become easier than ever due to the advancement in satellite remote sensing sensors. VHR images provide rich spatial details for characterizing objects on the ground. For this reason, they have been widely applied in land-cover and land-use classification [1], urban functional zone understanding [2], urban management [3], building roof modelling [4], large-scale terrain classification [5], and object extraction and monitoring [6, 7]. Objects in the land-cover classes tend to show high intra-class discrepancy and inter-class consistency, leading to challenges in image interpretation. Geographic Object-based Image Analysis (GeOBIA) has been proven to be a useful approach to address this issue by transitioning image interpretation from pixel-level to object-level and by partitioning an entire satellite image into meaningful geo-objects [8]. Image segmentation plays a crucial role in GeOBIA as well as other image analysis workflows. Geo-objects are generally clustered with adjacent pixels with similar characteristics such as spectral reflectance. Many efforts have been made to design efficient and precise segmentation methods. However, these methods fail to produce desirable segmentation results, as they tend to exhibit segmentation bias, including over-segmentation and under-segmentation errors, especially when they are applied to large-area VHR images with objects of different sizes. It is thus paramount to design more accurate and efficient segmentation algorithms that can be applied to a wide range of applications.

To satisfy the high segmentation quality demanded by diverse applications, hybrid segmentation methods were proposed based on Spilt-and-merge (i.e., region-merging). Spilt-and-merge strategy tolerates over-segmentation as segments can be merged into objects. Following Spilt-and-merge, many efforts have been made to initialize over-segmentation results and further merge these over-segmented regions into meaningful geo-objects by learning discrepancies between neighbour geo-object pairs [9]. Region-merging involves three key steps: 1) initializing over-segmentation, 2) building a graph model based on the region adjacency graph (RAG) and the nearest neighbour

graph (NNG) [10], and 3) merging the most-similar segment pairs according to the least weight edge extracted from the RAG-NNG. Fig.1 illustrates the segmentation results of the proposed method against state-of-the-art (SOTA) hybrid segmentation methods based on region-merging.

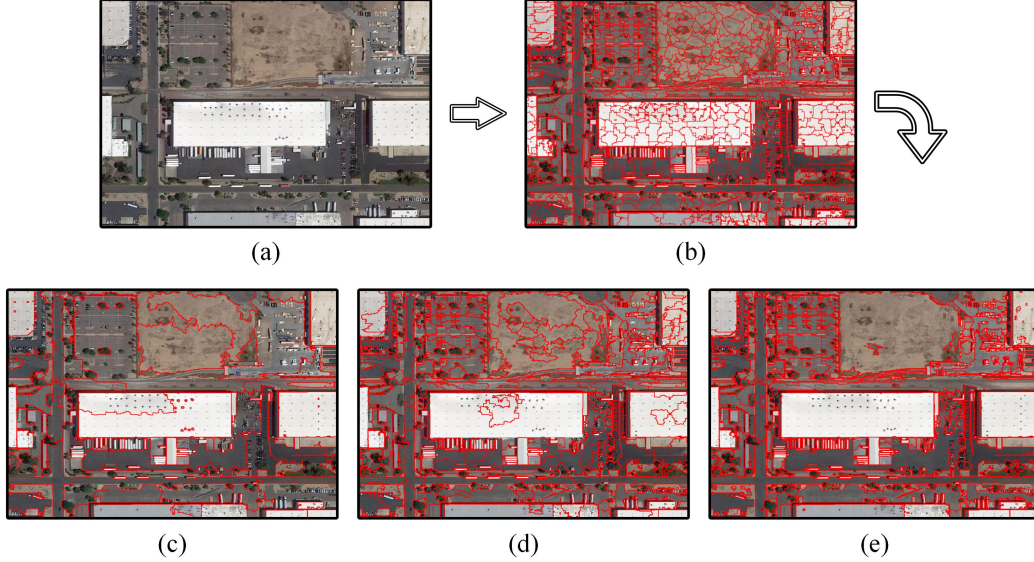


Figure 1: Comparison of different hybrid segmentation methods in region-merging. (a) Original remote sensing image. (b) Initial primitive segments. (c) Region-merging results of SOTA method Zhang2013 [11]. (d) Region-merging results of SOTA method Yang2017 [12]. (e) Region-merging results of the proposed method DeepMerge.

Hybrid region-merging via RAG-NNG can be implemented in an unsupervised or supervised manner. For unsupervised methods, users need to select a proper scale parameter (i.e., the threshold or the stopping rule) designed to stop merging by measuring discrepancy (or similarity) between adjacent segment pairs. Different merging criteria can lead to different scale parameter values, leading to difficulty in the selection of the optimal scale parameter. Their segmentation results are far from satisfactory. Supervised segmentations are designed to measure the discrepancy or similarity among segments via combined features between segments and reference objects. However, supervised segmentations face challenges when they are applied to large VHR images. Most of the existing supervised methods are designed for a single scene, failing to generalize to other scenes due to the discrepancy in geo-objects' characteristics. To process large VHR images, many studies split

the image into smaller adjacent sub-images (often called tiles), which are segmented independently. However, the geo-objects located on the edges between tiles are divided, introducing segmentation problems that we refer to as edge effect.

As discussed above, supervised and unsupervised methods both suffer from the large variance of geo-object sizes, the proper selection of scales, low segmentation accuracies, and edge effects. To address these challenges, we propose a deep learning-based region-merging method (DeepMerge) to handle segmentation in large VHR images. To our best knowledge, this is the first effort to combine region-merging with deep learning for image segmentation to obtain results in vector format. The key contributions of our study are the following:

- A deep learning-based region-merging method was designed to enhance segmentation of large VHR images. The proposed method results in high-accuracy segmentations compared to SOTA methods, correctly segmenting both small and large objects.
- To facilitate sample collection, we designed a user-friendly graphical interface. A skilled-operator can select at least 10,000 training sample pairs in a working-day. This allows users to collect large training sets.
- We introduce a multi-level data embedding module and segment-based feature module to extract inputs for a Vision Transformer network. These two modules can capture local, global, and object information, learning the similarity and discrepancy between adjacent segments. Based on the ability to learn region similarity, objects located on the boundaries of tiles can be merged.

## 2. Related works

Image segmentation is an essential step in remote sensing image analysis workflows; its goal is to cluster adjacent similar pixels into meaningful geo-objects. A great number of efforts have been made to improve the segmentation quality of remote sensing images, such as the development of simple linear iterative clustering [13], superpixels extracted via energy-driven sampling [14], mean-shift [15], multi-resolution segmentation [16]. Contour-based methods are an important branch of segmentation methods focusing on the extraction of object boundaries [17, 18, 19]. However, the segmentation



methods that rely on a single strategy usually fail to meet the requirement of high-quality segmentation. Thus, region-merging based segmentation have received wide attention. In this section, we review related works concerning the optimization of scale parameters, merging criteria, vision Transformers, and Siamese networks.

### *2.1. Scale parameter optimization in image segmentation*

Efforts have been made to optimize scale parameters in region-merging methods. The segmentation output varies by setting different global scales in the investigated area. Low scale results in small-area segments, benefiting the segmentation of small geo-objects; however, large objects tend to contain multiple regions, leading to over-segmentation errors. The manual-optimal scale is often determined by a trial-and-error process, causing uncertainties in segmentation results [1, 20]. Therefore, scholars developed automatic and self-adaptive scale optimization methods. The majority of region-merging algorithms calculate the homogeneity in geo-objects and the heterogeneity between geo-objects to determine the optimal scale for geo-objects. For example, an automated approach to parameterizing multiscale image segmentation was proposed to detect scale transitions in geo-object relying on the local variance [21]. [22] proposed a spatial and spectral statistics-based scale parameter selection for object-based information extraction using an average local variance graph. [23] developed a general stepwise evolution analysis framework for optimal scale parameter estimation using local variance and Moran’s I, a measure of spatial autocorrelation. In order to better segment geo-objects of various sizes, a scale-variable segmentation method was proposed where scale parameters are adaptively estimated [24]. To obtain the objective-adaptive scale for each geo-object, [25, 26] proposed object-specific optimization strategies using hierarchical tree structures of multiscale segmentation.

### *2.2. Merging criteria*

Merging criteria have been regarded as another important component that determines the segmentation results. To enhance the quality of segmentation, a supervised classic watershed segmentation method was improved via multispectral gradient in [27]. Furthermore, [28] utilized a graph-cutting heuristic method to accelerate the Minimum Spanning Tree-based algorithm. [29] developed an unsupervised image segmentation and evaluation and refinement using weighted variance and Moran’s I in a series of scales.

[9, 11, 30, 31] introduced edge strength, compactness, and the feature of standard derivation into the merging criteria. [32] developed a multiscale segmentation method to achieve results through stepwise refinement guided by area and boundary features. Local spectral statistics was used to measure the homogeneity and heterogeneity between segments [33]. To delineate dune-field landscape patches, [34] proposed a new method that integrates multisource features that represent dune-field landscapes at multiple scales. [31] viewed the region-merging process as a classification process and trained a random forest using segment-based features of geo-objects. However, the segment-based features failed to fully capture the details of geo-objects, leading to the segmentation failure of complex geo-objects.

### 2.3. Rationale of Vision Transformers

The vision Transformer is a deep learning model able to capture long-range pixel dependencies based on the self-attention mechanism [35]. Inspired by human visual concentration, the self-attention mechanism focusses the attention on important information, thereby saving resources and extracting accurate information in a rapid manner. The vision Transformer is essentially an Encoder-Decoder structure composed of multi-head modules using an attention mechanism. Eq.2 depicts the process of the attention mechanism.  $V(=AW^v)$  is the output of the input  $A$  linear transformed by the weight  $W^v$ . In the visual image processing,  $A$  is a one-dimensional vector obtained by dividing the image into equal-sized patches like checkerboards, and then applying a convolution with the kernel size the same as the patch on the patches. The *softmax* function plays the role of scorer for  $V$  based on query ( $Q = AW^q$ ) and key ( $K=AW^k$ ), where  $W^q$ ,  $W^k$  are the weights for updating in the backpropagating process,  $Q$  and  $K$  are two special matrices used for searching the importance of pixels.

$$Attention(Q, K, V) = softmax\left(\frac{QK^T}{\sqrt{d_k}}\right)V \quad (1)$$

$$softmax(z_i) = \frac{\exp(z_i)}{\sum_{j=1}^K \exp(z_j)} \quad (2)$$

where  $d_k$  is the dimension of  $K$ . The output of the attention module, named head, contains scored information in  $A$ . The above process is the basic principle of the attention mechanism. The *softmax* function applies the standard exponential function to each element  $z_i$  of the input vector  $z$  and normalizes

these values by dividing by the sum of all these exponentials; this normalization ensures that the sum of the components of the output vector  $z$  is 1. To accelerate the convergence of the model, the multi-head attention module is applied in the transformer, which is defined in Eq.3 and Eq.4:

$$head_i = Attention(AW_i^Q, AW_i^K, AW_i^V) \quad (3)$$

$$Multihead(Q, K, V) = concat(head_1, head_2, \dots, head_h)W^o \quad (4)$$

where  $i$  is the indicator for counting heads, the projections are parameter metrics  $W_i^Q \in R^{d_{model} \times d_k}$ ,  $W_i^K \in R^{d_{model} \times d_k}$  and  $W_i^V \in R^{d_{model} \times d_k}$ .  $W^o$  denotes the parameter metrics of the linear addition ( $concat(., \dots, .)$  in Eq.4) of multiple heads. The vision Transformers is a combination of multi-head modules. It can concatenate one-dimensional randomly initialized vector (class token) and the embedded features from images in the training model. In the training process, the class token can learn local pixel information and the global positional relationships. In this paper, we proposed an improved vision Transformer, which is described in the next section.

### 3. Methodology

#### 3.1. Outline of the proposed method

The proposed DeepMerge is the first to integrate deep learning and region-merging to achieve desirable segmentation in VHR remote sensing images. Fig.2 summarizes the workflow of DeepMerge. We first partition the original image into tiles of the same size. These tiles are then over-segmented into the primitive segments by a standard segmentation method. Then we utilize a Siamese network [36, 37] to learn the similarity between neighbouring segments. The network is trained using a training set composed of positive and negative samples. Pairs of adjacent segments of the same object are called positive samples. On the contrary, pairs of neighbouring segments of different objects are negative samples. To train the network, we manually select positive and negative samples, train the proposed Siamese deep learning model, and measure similarities between adjacent segments. After training the Siamese networks with positive and negative samples, the network is able to measure the similarity between adjacent segments. Finally, the RAG-NNG model, iteratively merges the most-similar segment pairs via the global best-merging strategy until the similarity of the least weight edge in

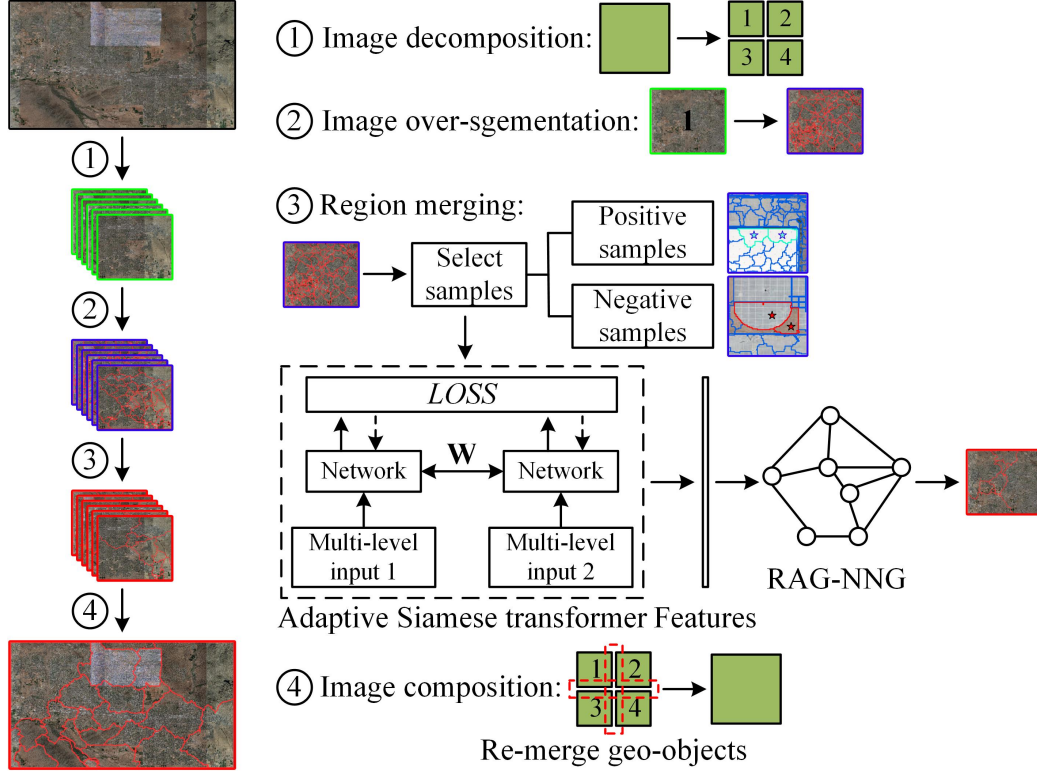


Figure 2: The workflow of the proposed DeepMerge for segmentation in high-resolution remote sensing imagery.  $W$  means shared weights

RAG-NNGs is higher than a user-defined threshold. Eventually, geo-objects are merged to obtain the final segmentation in a vector format.

We recommend multi-resolution segmentation (MRS), a region-growing segmentation method that follows the minimum heterogeneity principle, as the initial segmentation method [16]. MRS has been proven to be efficient in generating initial segmentation results as polygons in a shapefile format [38]. Of course, other segmentation methods can also be used as the initial segmentation method in our framework.

We describe the multi-level inputs, details of the proposed network, and the feature updating strategy for the merging process in the following sections. All codes run either in C# (sample selection software, multi-level inputs extraction, RAG-NNG model) or Python languages (adaptive Siamese transformer model and RAG-NNG model). We open-source the code at the

link: <https://pan.baidu.com/s/1BVQ24iQZJJpWHytCN2jyKw?> (Extraction code: 1234).

### 3.2. Sample collection for training DeepMerge

To train the transformer-based Siamese network, we manually collected samples according to the following steps. We visually analysed the segments in the initial over-segmentation results, and determined the dominant categories in the study areas. Then, we selected neighbouring segments (Fig.3a) with high homogeneity serving as positive samples (Fig.3b), and neighbouring segments of different categories serving as negative samples (Fig.3c). It is worth noting that we need to collect more negative than positive samples to account for the large variety of possible discrepancies of two different regions. In VHR images, one object may contain high heterogeneous segments and different adjacent segments can contain similar pixels, leading to segmentation errors. Therefore, it is necessary to select many samples of both situations. In addition, we have to focus on similar neighbouring segments in different categories, such as rivers and vegetations, asphalt roads and shadows, and vegetations and roads. We developed a user-friendly graphical interface for collecting the training samples, which can automatically record indexes of sample pairs selected by operators. Therefore, a skilled-operator can select at least 10,000 sample pairs in a working day, greatly improving work efficiency.

The Siamese network requires image patches as inputs, similar to standard deep learning models. However, the samples collected above for the proposed model are segment pairs, i.e., positive and negative samples with varying shapes and sizes, as shown in Fig.3. It leads to an input gap between segment samples and the proposed model requirement. To overcome the disparity between segment samples and the requirement for square patches, we represent segments using patches with global and local information. Thus, a binary tree sampling method (BTS), as a crucial step in Object-based convolutional neural networks [20, 39] is implemented to generate suitable inputs that can be fed into the proposed model from segment samples [40] to improve the segment identification quality. The original BTS is able to partition a segment into sub-segments by recursively dividing the segment into two parts until a user-defined threshold is reached. Based on the positions of sub-parts, multi-level data can be extracted in an adaptive window size. Fig.4 demonstrates how BTS works. For more information, please refer to [40].

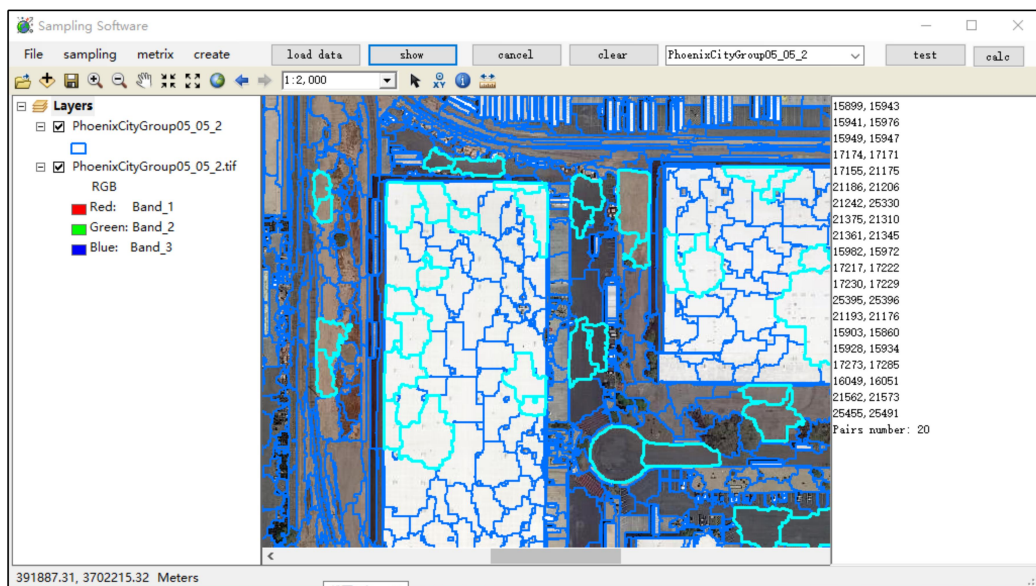


Figure 3a: Sample collection software.

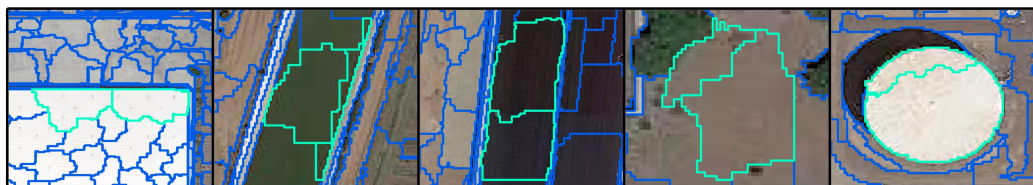


Figure 3b: Examples of positive samples.

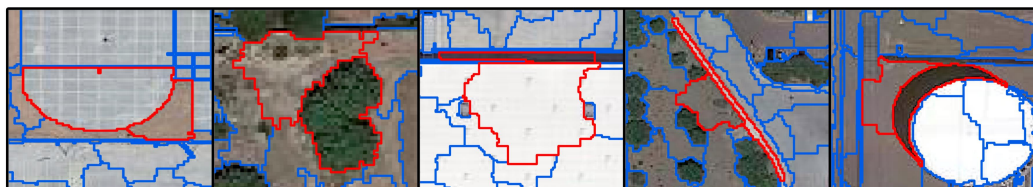


Figure 3c: Examples of negative samples.

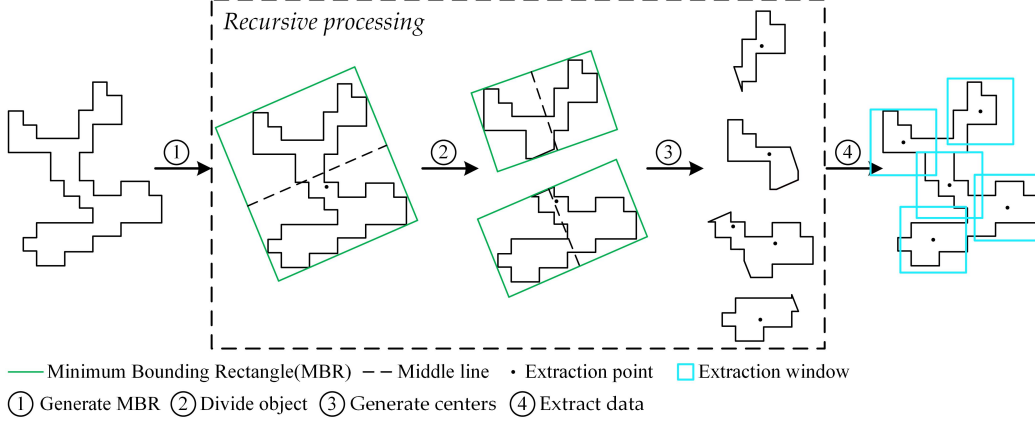


Figure 4: The basic theory about BTS.

The number of the threshold and the extraction window size are the key issues in the sampling procedure. Thus, we improve BTS by developing an automatic strategy. According to [40], up to three positions are needed to extract information for the representation of a segment. The window size is determined by the ratio of the intersection of the windows and the segments. Therefore, each segment corresponds to different window sizes. In order to obtain local and global information of segments, we designed extraction windows in four levels ( $P_1$ ,  $P_2$ ,  $P_3$ , and  $P_4$ ). The automatic strategy is summarized as follows.

*Seg* is a primitive segment to extract square patches. The red stars in *Seg* are the positions for extracting square patches (i.e., the red middle star in Fig.5 is the *Pos*). *ExtractPatch(.)* is a function applied to extract a square *patch* with the *Pos* as the centre and the initial side length of 5 pixels. The intersection area calculated by function *Intersect(.)* between *Seg* and *patch* is *intersect\_area*. We iteratively increase the width of the square patch by 5 pixels. The *intersect\_area* will increase accordingly. Meanwhile, the *ratio* of the intersection to the current patch will decrease from 100%. When the *ratio* is firstly lower than 90%, the current patch will serve as  $P_1$ . When the *ratio* is smaller than 30%, the current patch will serve as  $P_2$ . Thus,  $P_3$  and  $P_4$  can define by *Pos* and width difference of  $P_1$  and  $P_2$  shown in the above pseudo codes. The 90% and 30% are defined by the human visual observation on the objects. We found that when the *ratio* approaches 90%, the current patch can capture most inner information without much external information. The balance information inner and external objects can be

---

**Algorithm 1:** multi-level input data generation

---

**input** : A primitive segment  $Seg$  and a centre position  $Pos$  for  
extracting image patches

**output:** Four patches  $P_1, P_2, P_3, P_4$  in four levels

```
1  $patch \leftarrow \text{ExtractPatch}(Pos, 5);$ 
2  $iter \leftarrow 0;$ 
3 while  $P_1, P_2 == null$  do
4    $intersect\_area \leftarrow Seg.Intersect(patch).area;$ 
5    $ratio \leftarrow intersect\_area / patch.area;$ 
6   if  $ratio \leq 0.90$  and  $P_1 == null$  then  $P_1 \leftarrow patch;$ 
7   if  $ratio \leq 0.30$  and  $P_2 == null$  then  $P_2 \leftarrow patch;$ 
8    $iter \leftarrow iter + 1;$ 
9    $patch \leftarrow \text{ExtractPatch}(Pos, 5 + iter \times 5);$ 
10  $P_3 \leftarrow \text{ExtractPatch}(Pos, P_2.width + (P_2.width - P_1.width));$ 
11  $P_4 \leftarrow \text{ExtractPatch}(Pos, P_2.width + 2 \times (P_2.width - P_1.width));$ 
12 final;
13 return  $P_1, P_2, P_3,$  and  $P_4;$ 
```

---



captured by the current patch when the ratio approaches to 30%. Note that other positions in Fig.5 share the same multi-level window sizes. Because the segments are of different shapes, the square patches extracted from each segment are also different.

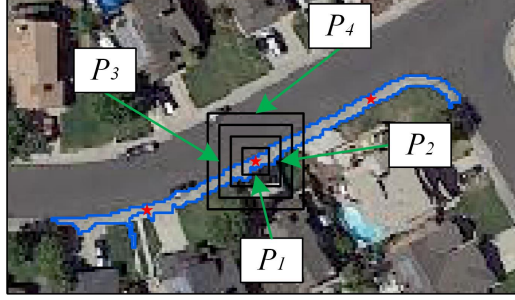


Figure 5: Multi-level input generation.

As most segments tend to be over-segmented, a geo-object can contain multiple segments. Thus, information from the  $P_1$  and  $P_2$  can sometimes only represent the object partially. To enhance the representation of global geo-objects, information from the  $P_3$  and  $P_4$  need to be extracted. In certain cases, some small segments are completely segmented without over-segmentation errors (see the blue geo-object in Fig.5). In this situation, the designed multi-level information strategy provides not only global information for better overall representation but also neighbouring information that improves the robustness of region-merging. Thus, small and large segments can be well-represented following the designed protocol.

### 3.3. Adaptive Siamese-transformer model

To learn the similarity and discrepancy between neighbouring segments, we propose an adaptive Siamese-Transformer model. Siamese network is used for supervised contrastive learning [37]. The basic structure of the Siamese network is presented in the dashed box shown in Fig.2. The features of negative and positive samples can be extracted by a weight-shared backbone network. The similarity and the discrepancy are obtained by the loss function that calculates the distance in the feature space. The backbone of the framework is an improved vision Transformer with a proposed multi-level embedding module and segment-based feature embedding module. Relying on the multi-head attention module, the structure of the improved transformer is shown in Fig.6.

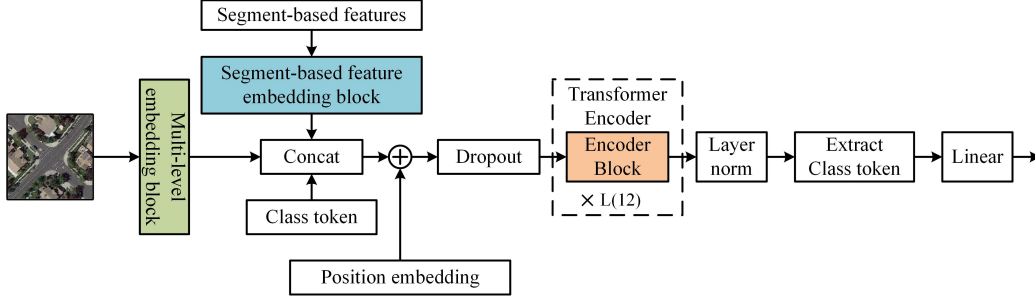


Figure 6: The architecture of the improved transformer in the DeepMerge.

The multi-level embedding module can encode multi-level input data in four levels to extract global and local information of segments. The segment-based feature embedding block can encode engineered features to integrate other deep features extracted by networks. The proposed two modules in the vision Transformer play a great role in learning similarity of segments. The blocks of the improved Transformer are shown in Fig.7 in detail.

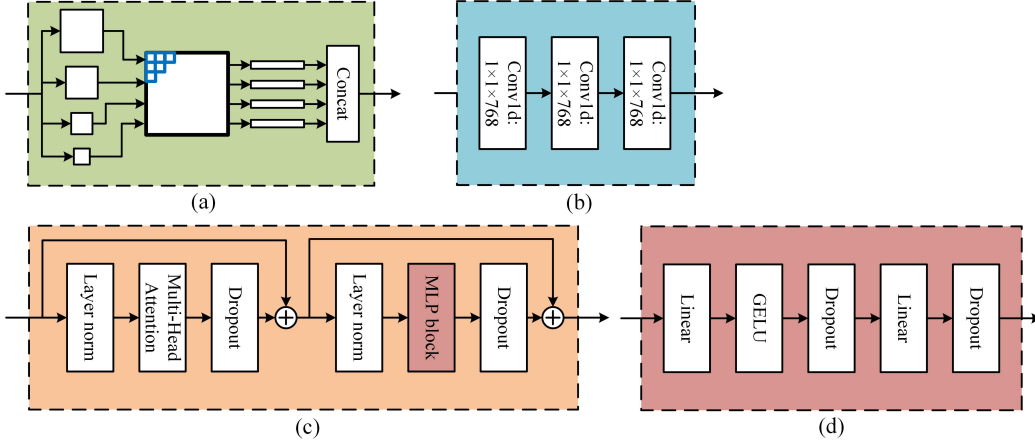


Figure 7: Blocks of the improved Transformer. (a) Multi-level embedding block; (b) Segment-based feature embedding block; (c) Encoder block; (d) MLP block.

The input images are embedded into  $196 \times 768$  features in a multi-level manner and concatenated with segment-based features and class tokens, forming the final extracted features. The dropout layer temporarily drops neurons from the network with a defined probability. The " $\times L(12)$ " means that the encoder block is repeated 12 times. The *layernorm* module nor-

malizes the distribution of the input data. The linear module is a one-layer fully connected network. MLP denotes the Multilayer Perception, and the gaussian error linear units (GELU) is the activation function [41]. In the improved transformer, the multi-level embedding module is designed to extract multi-level features. Four-level patches ( $P_i = \{P_1, P_2, P_3, P_4\}$ ) at the same location (described in Section 3.2) are embedded as follows:

$$O_i = \text{Conv2d}(\text{Resize}(P_i, 2^{i+1} \times 7), 2^{i+1}) \quad (5)$$

$$EF = \text{Flatten}(\text{Concat}(O_i)) \quad (6)$$

where  $P_i$  is resized with  $2^{i+1} \times 7$  in length, and then convolved with  $2^{i+1}$  filters into  $O_i$ .  $\text{Conv2d}(\cdot)$  is a two-dimensional convolution function. The function  $\text{Resize}(\text{size1}, \text{size2})$  can resize an image with size of  $\text{size1}$  into  $\text{size2}$ . Further, all  $O_i$  are concatenated and flattened ( $\text{Flatten}(\cdot)$  function) into two-dimensional vectors with a size of  $196 \times 768$ . Four-level patches at the same location are extracted by the BTS (Fig.4 and Fig.5). The sizes of the patches are respectively  $224 \times 224$ ,  $112 \times 112$ ,  $56 \times 56$ , and  $28 \times 28$ . The blue boxes in Fig.7a contain a total of 768 two-dimensional convolution filters with  $32 \times 32$ ,  $16 \times 16$ ,  $8 \times 8$ , and  $4 \times 4$  in size, respectively. Thus, each patch can be embedded into a total of  $49 \times 768$  features. After concatenating the four-level patch features, class token, and embedding segment-based features, the output is a two-dimensional feature with  $198 \times 768$  in size.

A total of ten features are designed for segment-based feature embedding module, including texture features, statistical features, shape features, standard deviation of each band, mean value of each band, the shape indicator, compactness, brightness, and border indicator. These features are computed considering the pixels within the segment. They capture different characteristics to assess region similarities with respect to deep learning features, which are calculated using a fixed window size. Their calculations follow:

$$\text{Mean}_i = \frac{1}{n} \sum_{j=1}^n v_j \quad (7)$$

$$\text{Std}_i = \sqrt{\frac{1}{n-1} \sum_{j=1}^n (v_j - \text{Mean}_i)^2} \quad (8)$$

$$\text{Shape} = \frac{l}{4\sqrt{C}} \quad (9)$$

$$Compactness = l\sqrt{n} \quad (10)$$

$$Brightness = \frac{1}{w^B} \sum_{i=1}^K w_i^B Mean_i \quad (11)$$

$$Border = \frac{l}{2(length + width)} \quad (12)$$

where  $i$  ( $i=1,2,3$ ) indicates the  $i$ th band,  $n$  denotes the segment size in pixels,  $v_j$  denotes the  $j$ th pixel value, and  $Mean_i$  denotes the mean value of the  $i$ th band in a region. The  $Std_i$  denotes the standard deviation of the  $i$ th band in a segment. The Shape denotes the shape indicator defined by the perimeter ( $l$ ) of a segment and the perimeter ( $C$ ) of the minimum bounding rectangle ( $MBR$ ) of a segment. The  $length$  and  $width$  are the long edge and the short edge of the  $MBR$ . The  $length$  and  $width$  are used to define the border indicator ( $Border$ ) and  $Compactness$ .  $K$  denotes the number of bands, and  $w_i^B$  denotes the related weight.

The output of the improved transformer is the class token after a linear transformation. The outputs are the features used for segment representation, and it will be used in calculating similarity in the RAG-NNG model. The features of positive sample pairs or negative sample pairs are extracted by the network and are supervised by the loss function. Given a pair of segments (left segment  $left$  and a right segment  $right$ ), the calculation of the loss function follows:

$$Loss = \alpha \left\| f_i^{left} - f_i^{right} \right\|_2 + (1 - \alpha) \max \left( 0, \left( \lambda - \left\| f_i^{left} - f_i^{right} \right\|_2 \right) \right) \quad (13)$$

where  $f$  means the feature vector in a segment,  $i$  indicates the feature item from the  $f$ .  $\alpha$  is a binary indicator (positive pair:  $\alpha=1$ ; negative pair:  $\alpha=0$ ).  $\lambda$  is a user-defined parameter that represents the cluster centre of the distance in feature space between negative sample pairs (we recommend  $\lambda=1$ ). The function  $\max(.,.)$  can return the maximum value from two parameters. In the proposed model, the distance in feature space between positive sample pairs should be close to 0, while the distance between negative sample pairs should be close to 1. Once the segment features are extracted by the proposed improved transformer, they further serve as the node features in the RAG-NNG model (described in Section 3.4).

### 3.4. Merging criteria and feature updating

Merging criteria are designed for calculating the similarity between segments, i.e., edge weight in the RAG-NNG model. We use the Euclidean distance of features from two neighbouring segments as the merging criteria in the proposed method:

$$MC = \left\| f_i^{left} - f_i^{right} \right\|_2 \quad (14)$$

where  $MC$  is the distance of two group features, which is the similarity of two segments, recorded as the weight of the connected edge in the RAG-NNG model. Conventional merging criteria updates edge weights of a newly merged segment by re-extracting features and re-calculating weights between the segment and its adjacent segments. However, deep features of a newly merged segment can cause inefficiency in region-merging if they are re-extracted by the pre-trained model. In the proposed DeepMerge, the features of a new segment are calculated via the weighted average of the original two features by Eq.15:

$$f_i^{left+right} = \frac{1}{M+N} \left( M f_i^{left} + N f_i^{right} \right) \quad (15)$$

where  $f_i^{left+right}$  are the features of new segments.  $M$  and  $N$  denote the feature vector weights of the segment *left* and *right*. *left* and *right* are the number of extracting centres by BTS in the segment *left* and *right*. Therefore, the feature vector weight of the new segment is  $M+N$ . In the initial segmentation results, the feature vector of a segment is the average of features extracted from multiple extracting centres by DeepMerge.

### 3.5. RAG-NNG model

Following the graph structure, RAG is constructed by taking the initial segments as nodes and the connections between segments as edges. Each node stores the features of the corresponding segment, and each edge stores the feature distance between two nodes at its ends. Fig.8 describes the concept of a RAG model in a hypothetical over-segmented case.

Based on the seven over-segmented segments (Fig.8a), a RAG (i.e., a non-directional graph) is constructed. The nodes in Fig.8b represent segments from the original segmentation, and the edges between nodes depict the connections between segments. The weight of an edge indicates the similarity between two neighbouring nodes, which is calculated by Eq.14. Supposing

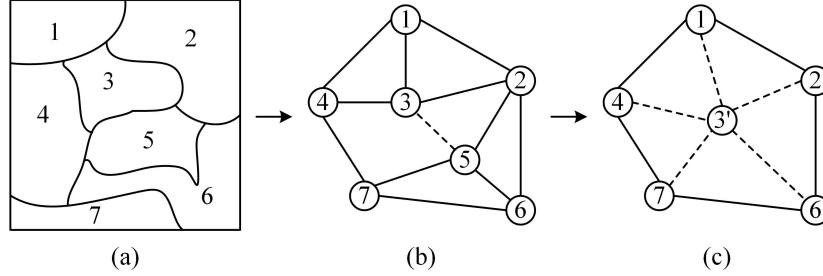


Figure 8: The construction of RAG-NNG and region-merging in a RAG-NNG model.

that the weight value of the dotted edge between *node 3* and *node 5* in Fig.8b is the smallest, indicating their high similarity, *nodes 3* and *5* are further merged into a new *node 3'* shown in Fig.8c. The weights of edges connected to *node 3'* are then updated by Eq.15. The RAG-NNG model Iteratively repeats these operations until the smallest weight is higher than a user-defined threshold.

For an image that covers a large geographic area, a great number of over-segmented segments tend to exist. To improve the efficiency of region-merging in RAG, NNG was developed. In a RAG-NNG model, each node has multiple edges connected to other edges, and the edge with the smallest weight value of the connected edges of one node is defined as the "direction" of the node. For example, the dotted edge is the "direction" of *node 3* (from *node 3* to *node 5*) (Fig.8b), and it is also the "direction" edge of *node 5* (from *node 5* to *node 3*). When two neighbouring segments own the same "direction" edge, a "cycle" is defined. In this case, *node 3* and *node 5* form a "cycle" (Fig.8b). NNG contains a minimum queue to store the "cycles", which pops the edge with the smallest value and further merges the related segments repeatedly. More details of RAG and NGG can be found in [9].

### 3.6. Segmentation accuracy estimation

To validate the segmentation performance of the proposed DeepMerge, three groups of accuracy assessment metrics are applied, considering over-segmentation, under-segmentation, and whole segmentation performance. The first group of metrics includes *precision*, *recall*, and *F* value [42]. The second group of metrics includes the global over-segmentation error (*GOSE*), global under-segmentation error (*GUSE*), and total error (*TE*) [43]. The third group includes potential segmentation error (*PSE*), number of segments ratio (*NSR*), and Euclidean distance (*ED2*) [44]. These measurement

metrics require polygon segmentation results and vectorized reference objects, which have been proven to be effective and robust for measuring the local and global segmentation performance from various aspects. The calculations of these metrics are presented in Table 1.  $S$  is the set of polygon segmentation results containing  $M$  segments  $\{S_1, S_2, \dots, S_M\}$ , and  $R$  is the set of polygon reference geo-objects containing  $N$  reference geo-objects  $\{R_1, R_2, \dots, R_N\}$ .  $|\ast|$  represents the area of a segment.  $R_{i,max}$  denotes the largest area reference geo-object related to the segment  $R_i$ , and  $R_{i,max}$  denotes the largest area segment related to the reference geo-object  $R_i$ .  $R_{ij}$  denotes the set of segments related to  $R_i$ .  $S_i \cap R_{i,max}$  is the intersection of  $S_i$  and  $R_{i,max}$ , and the  $S_i \cup R_{i,max}$  the union of them. The difference set  $|R_i \setminus S_{i,max}|$  contains pixels in  $R_i$ , but not in  $S_{i,max}$ .  $\alpha$  is set as 0.5. The  $\uparrow$  means higher values with better performance and vice versa for the  $\downarrow$ .

Assessment metrics	Formulas	Range	Trend
	$ S  = \sum_{i=1}^M  S_i $		
<i>precision</i>	$precision = \sum_{i=1}^M  S_i \cap R_{i,max}  /  S $	[0,1]	$\uparrow$
	$ R  = \sum_{i=1}^N  R_i $		
<i>recall</i>	$recall = \sum_{i=1}^N  R_i \cap S_{i,max}  /  R $	[0,1]	$\uparrow$
<i>F</i>	$F = 1 / \left( \alpha \frac{1}{p} + (1 - \alpha) \frac{1}{r} \right)$	[0,1]	$\uparrow$
<i>GOSE</i>	$GOSE = \frac{1}{ R } \sum_{i=1}^N  R_i  \frac{ R_i \setminus S_{i,max} }{ R_i  - 1}$	[0,1]	$\downarrow$
<i>GUSE</i>	$GUSE = \frac{1}{ R } \sum_{i=1}^N \min( R_i \cup S_{ij}  \setminus  R_i \cap S_{ij} ,  R_i )$	[0,1]	$\downarrow$
<i>TE</i>	$TE = GOSE + GUSE$	[0,2]	$\downarrow$
<i>PSE</i>	$PSE = \frac{1}{ R } \sum_{i=1}^N  S_{i,max} \setminus R_i $	$[0, +\infty]$	$\downarrow$
<i>NSR</i>	$NSR = \frac{1}{N} abs(N - V)$	$[0, +\infty]$	$\downarrow$
<i>ED2</i>	$ED2 = \sqrt{(PSE)^2 + (NSR)^2}$	$[0, +\infty]$	$\downarrow$

Table 1: Assessment metrics used for segmentation accuracy estimation.

## 4. Experimental Results

### 4.1. Dataset

The dataset used in this study covers nine cities that belong to the Phoenix city cluster, Arizona, U.S., including Phoenix, Glendale, Scottsdale, Tempe, Mesa, Chandler, Peoria, Surprise, and Goodyear. The images are composites from Google Earth [45] with a variety of sensors (e.g., WorldView, QuickBird, IKONOS, etc.) captured at different times. The image is  $182,272 \times 102,626$  pixels (covering  $5,660 \text{ km}^2$ ) with 0.55-meter resolution and RGB bands encoded as 8-bit integral values. A variety of scenes are included, e.g., urban residential zones, urban green spaces, industrial zones, rural farmlands, water areas, and bare lands (Fig.9).

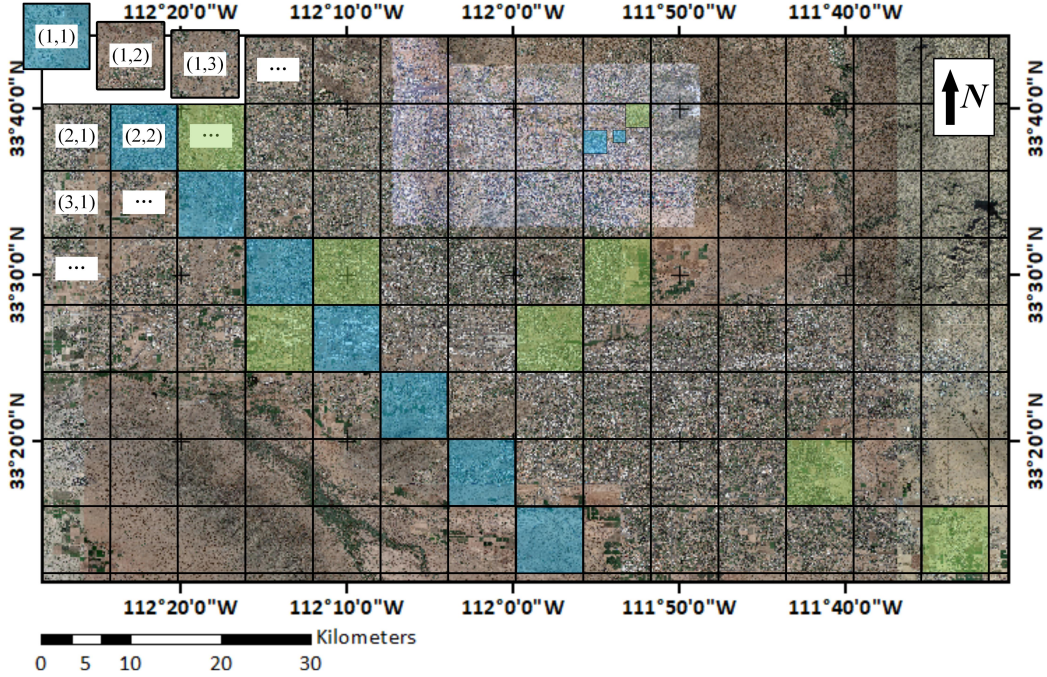


Figure 9: The study area of the Phoenix city cluster. The translucent blue tiles are used for training and the green tiles are used for accuracy assessment.

We partition the image into a total of 135 tiles encoded by row and column numbers (Fig.9). The average size of a tile is  $12,800 \times 12,800$  pixels. The training of the proposed DeepMerge requires negative and positive samples. In the Phoenix dataset, negative and positive pairs are selected in the



tiles with translucent blue masks, as shown in Fig.9. A total of 71,948 segment pairs (54,945 negative sample pairs and 17,003 positive sample pairs) involving 92,421 segments, are manually collected as training data. There is a total of 47,995,928 segments in the whole study area. The training data accounts for 0.19% ( $=92,421/47,995,928$ ) of the total number of segments.

To assess the performance of region-merging strategies, a total of 3,776 polygons are manually digitized as reference geo-objects. To validate the transferability of DeepMerge, the reference geo-objects, covering a variety of land uses (Fig.10), are selected in the green mask tiles in Fig.9.



Figure 10: Examples of reference geo-objects.

The proposed DeepMerge and other competing methods are implemented in C# and python programming language and tested on a computer with Windows 10 operation system, an intel i7-10700 CPU (2.9GHz), 32GB RAM, and an NVIDIA GPU (RTX 2080ti).

#### 4.2. Region-merging results

For consistency, we set the shape, compactness, and scale parameters of MRS for initializing over-segmentation as 0.5, 0.5, and 25. Too many segments can lead to low efficiency of region-merging. The MRS with these parameters applied to segment minimum geo-objects in the dataset with little over-segmentation errors, maintaining a balance between over-segmentation errors and reducing segment number. Relying on the same initial over-segmentation and the same RAG-NNG model, ten bottom-to-top supervised and unsupervised methods are selected as competing algorithms, including MRS [16], Zhang2013 [11], Zhang2014a [9], Zhang2014b [24], Chen2015 [46],

Hu2017 [47], Yang2017 [12], Shen2019 [25], Zhang2020(fine and coarse) [26], Su2020 [31], and Lv2021 [1]. Except for MRS, other competing methods are denoted via the first author’s family name plus the article publication year. These methods differ in optimization strategies, including merging criteria (e.g., edge penalty), object optimization, scale sets, and supervised segmentation. Diverse merging criteria suggest different scale parameters. Some multiscale segmentation methods (Zhang2013 and Zhang2014a) set scale parameters by trial and error. The scale parameters in Zhang2014b, Chen2015, Yang2017, Su2020, and Lv2021 are set as recommended. Hu2017, Shen2019, and Zhang2020 (fine and coarse) automatically generate specific objects with optimized scales, where Zhang2020 can produce coarse and fine segmentations at the same time. In our experiments, we set optimal scale value of DeepMerge to 0.6.

The segmentation performances of DeepMerge and other competing methods are shown in Table 2. A sensitivity analysis of the scale parameter is reported in Section 4.3. The *precision*(0.9772) of the segmented results from MRS, the initial segmentation approach, is the highest, and the *GUSE* value (0.0346) and the *PSE* value (0.0142) of MRS are the lowest among all investigated methods. These three metrics are closely related to over-segmentation errors. In general, higher precision, lower *GUSE*, and lower *PSE* values indicate stronger over-segmentation errors and weaker under-segmentation errors. We notice that the proposed DeepMerge achieves the best performance in six metrics compared with other methods, especially in *F*, *TE*, and *ED2*. The *F* value of DeepMerge is 0.9446, an improvement of 0.6246 compared to the initial segmentation and 0.0981 higher than Zhang2014a, the second-best method (*F* value: 0.8465). The *TE* and *ED2* values (0.0962 and 0.8989) of the DeepMerge are the lowest, suggesting small segmentation errors. Note that the proposed DeepMerge, among all competing algorithms, achieves high precision and recall values at the same time, indicating its superiority and robustness. Compared to MRS, the *recall* value of DeepMerge is significantly improved from 0.1913 to 0.9419, scarifying only 0.0298 in *precision*.

Example segmentation results of the investigated algorithms are presented in Fig.11, where three typical landscape types are selected: 1) urban residential areas (Fig.11a), 2) rural industrial zones (Fig.11b), and 3) rural green spaces (Fig.11c). We notice that results from MRS contain notable over-segmentation errors. Relying on the results from MRS results, other investigated methods started to generate their optimized segmenta-

Method	precision $\uparrow$	recall $\uparrow$	F $\uparrow$	GOSE $\downarrow$	GUSE $\downarrow$	TE $\downarrow$	PSE $\downarrow$	NSR $\downarrow$	ED2 $\downarrow$
MRS	<b>0.9772</b>	0.1913	0.3200	0.1028	<b>0.0346</b>	0.1375	<b>0.0142</b>	11.5456	11.5456
Zhang2013	0.9540	0.4233	0.5864	0.1392	0.0431	0.1823	0.0152	4.1668	4.1669
Zhang2014a	0.9568	0.7590	0.8465	0.1247	0.0459	0.1706	0.0152	6.0196	6.0196
Zhang2014b	0.9714	0.3288	0.4913	0.1246	0.0394	0.1641	0.0157	6.5400	6.5400
Chen2015	0.9657	0.5954	0.7366	0.1762	0.0504	0.2265	0.0167	6.4150	6.4150
Hu2017	0.8870	0.6504	0.7505	0.1164	0.0483	0.1647	0.0156	1.3374	1.3375
Yang2017	0.7062	0.8179	0.7580	0.0610	0.1370	0.1980	0.0152	2.8747	2.8748
Shen2019	0.9733	0.3154	0.4764	0.1145	0.0819	0.1964	0.1062	10.3633	10.3639
Zhang2020(fine)	0.9700	0.4624	0.6262	0.1387	0.0406	0.1793	0.0148	3.7503	3.7503
Zhang2020(course)	0.9586	0.5150	0.6700	0.1283	0.0469	0.1751	0.0157	2.5254	2.5255
Su2020	0.9699	0.3860	0.5522	0.1606	0.0390	0.1996	0.0144	7.9396	7.9396
Lv2021	0.7346	0.8737	0.7981	0.0903	0.0563	0.1466	0.0146	6.1435	6.1436
DeepMerge	0.9474	<b>0.9419</b>	<b>0.9446</b>	<b>0.0431</b>	0.0531	<b>0.0962</b>	<b>0.0142</b>	<b>0.8988</b>	<b>0.8989</b>

Table 2: Region-merging performance of the proposed DeepMerge and other competing methods.

tions. We observe that the segmentation results of DeepMerge are satisfactory and superior to the others. Almost all house outlines, road boundaries, green spaces, and even sidewalk boundaries are precisely delineated by DeepMerge (Fig.11a). Zhang2014a and Hu 2017 also achieve good performances, however, with discontinuous roads. The excellent performance of DeepMerge is also demonstrated in Fig.11b, where geo-objects vary greatly in size, texture, shape, and spectrum. DeepMerge successfully delineates large areas of bare land, factory buildings, roads, and even individual trees. Yang2017a and Hu2017 also present satisfactory segmented results, but some over-segmentation errors still exist (see the spots in buildings of Yang2017a and the bare lands of Hu2017). The above qualitative results well support the robustness of the proposed DeepMerge.

#### 4.3. Segmentation results at different scales

The final segmentation results of the proposed method can be derived by setting different scales. The segmentation evaluation metrics of *precision*, *recall*, *F*, and *GOSE*, *GUSE*, and *TE* of the proposed DeepMerge are presented in Fig.12, where the scales are set as 0.01, 0.1, 0.2, 0.3, 0.4, 0.5, 0.6, 0.7, 0.8, 0.9, and 0.99. The curve of *precision* (red line in Fig.12a) tends to decrease slowly for scales from 0.0 to 0.7. After 0.7, however, the *precision* decrease sharply with the further increase of scales. The *recall* value of the proposed DeepMerge increases sharply when the scale is above 0.2. In comparison, the *F* values first increase and then decrease with the continuous increase of scales. The highest *F* value is achieved when the scale is 0.6, where all three curves intersect each other. The *GOSE* values present a decreasing trend

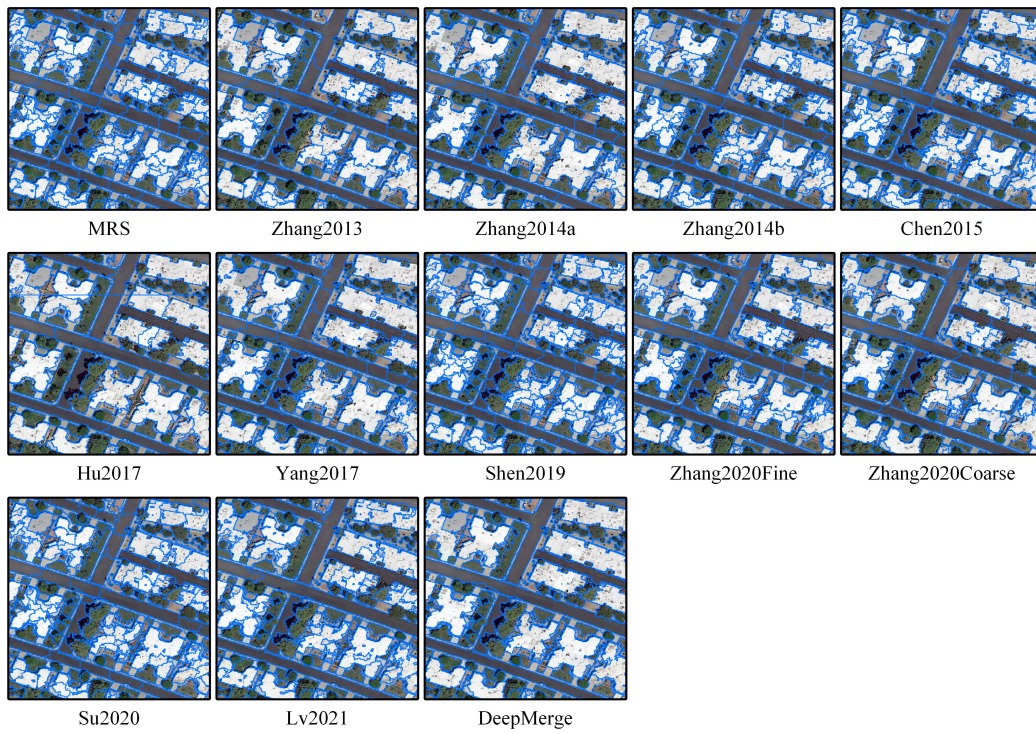


Figure 11a: Region-merging results in urban residential areas.



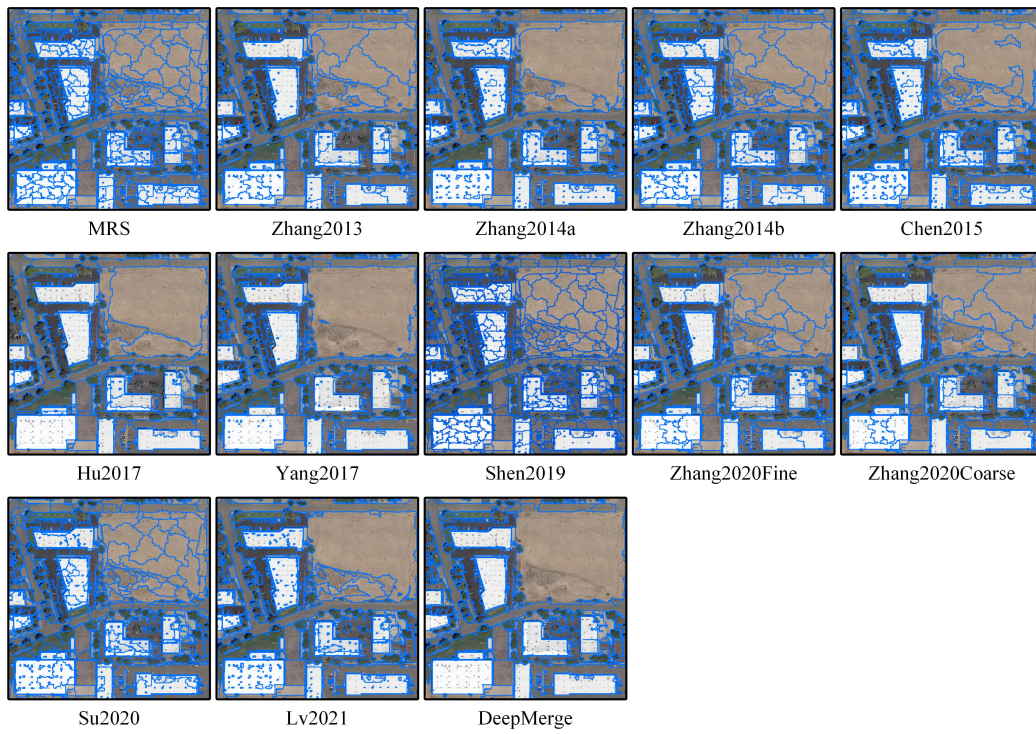


Figure 11b: Region-merging results in rural industrial zones.

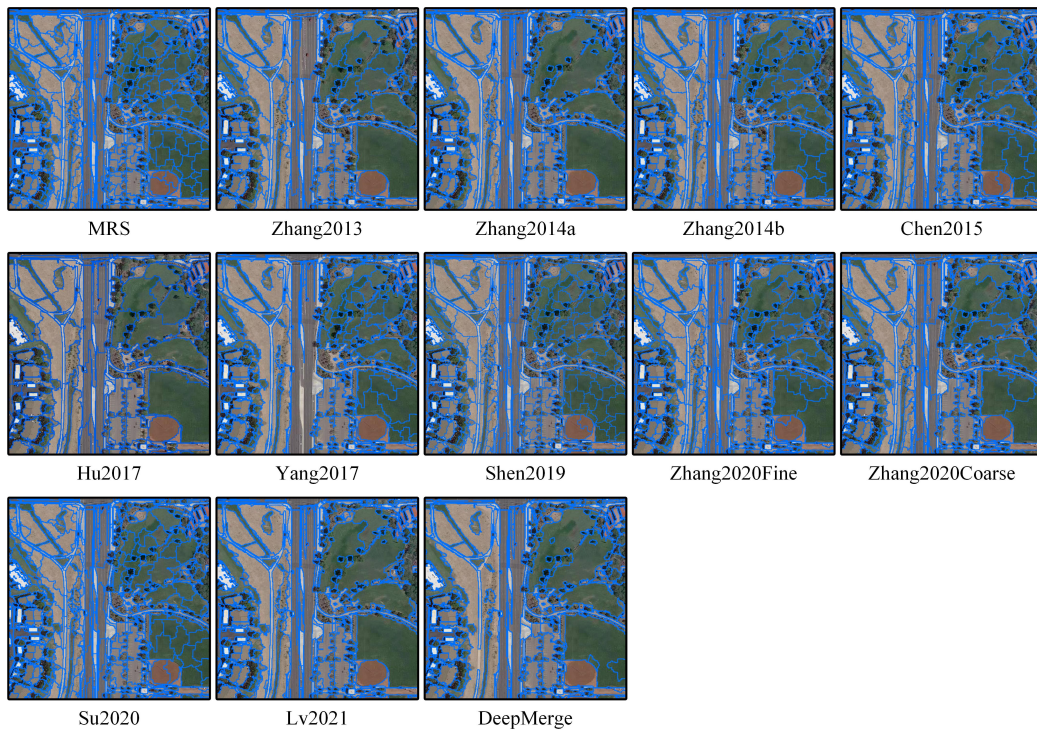


Figure 11c: Region-merging results in and rural green spaces.

as the scale increases (Fig.12b). In contrast, the *GUSE* values present an increasing trend as the scale increases. The *TE* values first decrease when the scale is between 0.0 and 0.8 and then increase sharply when the scale is above 0.8. The lowest *TE* value is achieved when the scale is 0.6. In general, the segmentation performance of DeepMerge varies with different settings of scales. The above results suggest that the optimal scale for DeepMerge is 0.6.

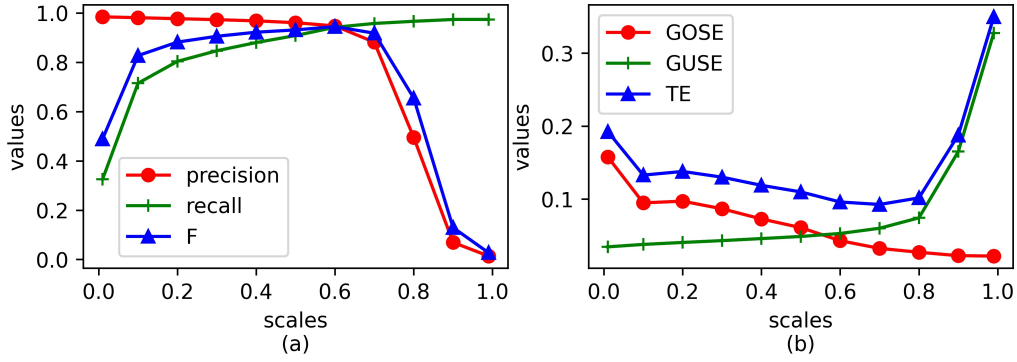


Figure 12: Segmentation performance of the proposed DeepMerge with different scale settings. (a) Performance curve by *precision*, *recall*, *F*. (b) Performance curve by *GOSE*, *GUSE*, and *TE* values.

#### 4.4. Image composition

Segmentation remains to be a challenge in large-area VHR images processing. To address the issue, the large image has to be divided into small-size tiles. Image composition aims to merge the regions in the boundaries of these tiles to solve the edge effect [48]. Fig.13 presents four segmentation results for four cross-tile segmentation results covering four different typical landscapes. Images in the first column of Fig.13 are the initial segmentation results from MRS, where green and red colours are used to distinguish segments from two different images, and the number of the first column images (such as (5,7) and (5,8) in the first image) denote the location of this scene in the Phoenix city cluster dataset (Fig.9). Images in the middle column are the segmentation results from DeepMerge without image composition. The image composition results of DeepMerge are presented in the last column. Fig.13a covers an industrial zone where factory buildings are concentrated with varying sizes, textures, and road materials. The scene in Fig.13b is similar to the one in



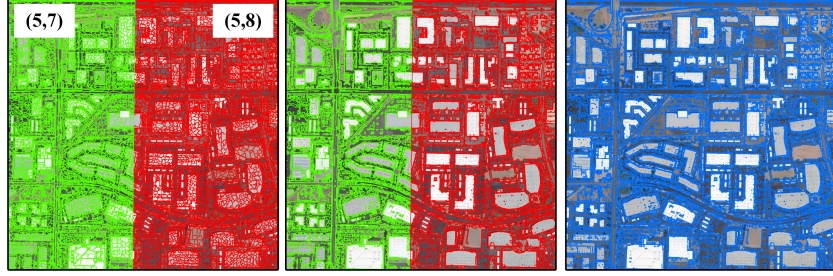


Figure 13a: Industrial zone with lots of factory buildings.

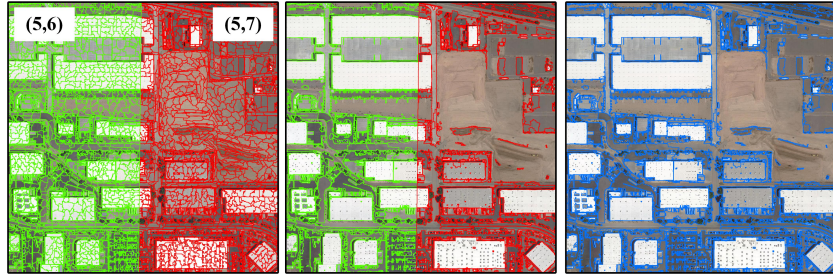


Figure 13b: Industrial zone and large bare soils.

Fig.11b with the addition of large bare soils across images. The segmentation results on the extensive green space in Fig.13c proves the excellent performance of the proposed method. The scene in Fig.13d contains lots of residential houses with continuous roads across two images.

We notice that the factory buildings with different sizes and textures located on the common edge of two images can be effectively merged via the proposed DeepMerge method, as shown in Fig.13a and Fig.13b. The asphalt roads and concrete roads can be successfully merged into continuous roads,

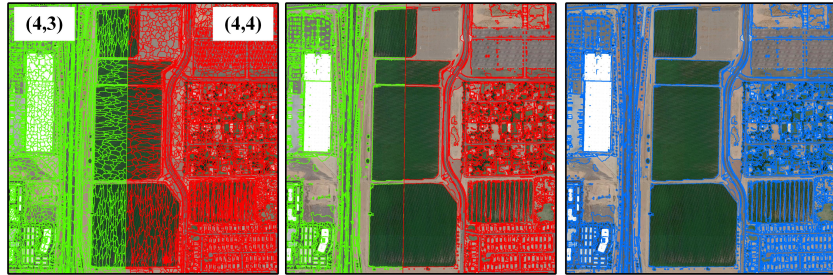


Figure 13c: Rural zone.





Figure 13d: Residential zone.

as demonstrated in Fig.13a, 13b, and 13d. As for bare soils and large green space in the 13b and 13c, the proposed DeepMerge is able to merge them into complete geo-objects. This shows the ability of the proposed method to generate complete segments of geo-objects of various sizes and result in superior region-merging performance.

#### 4.5. Ablation experiment

The parameters involving margin value, training epoch number, batch size, and learning rate of DeepMerge are set to 1.0, 50, 20, and 0.001, respectively. The quantitative segmentation measures via nine evaluation metrics of ablation experiments are described in Table 3. “TF” denotes a model with direct implementation of a native vision Transformer (TF) without any adaptations. As expected, the TF model achieves unsatisfactory performance as it fails to consider the sizes of geo-objects. “TF+MLE” denotes a model with a multi-level embedding module (MLE) added to the TF. The results suggest improved performance, evidenced by the increased *recall* and *F* values and decreased *GOSE*, *TE*, *NSR*, and *ED2* values, proving the ability of multi-level embedding module to improve the segmentation performance. “TF+MLE+SFE” denotes a model with MLE and segment-based feature embeddings (SFE) added to the TF, which has achieved significantly improved performance over TF and TF+MLE, demonstrating that the segment-based feature embedding module can enhance the segmentation quality.

## 5. Discussion

The proposed DeepMerge only takes 0.19% of the total number of segments as training to achieve desirable segmentation results. The optimal scale parameter value stabilizes between 0.4 and 0.7 in different landscapes.

Method	precision $\uparrow$	recall $\uparrow$	F $\uparrow$	GOSE $\downarrow$	GUSE $\downarrow$	TE $\downarrow$	PSE $\downarrow$	NSR $\downarrow$	ED2 $\downarrow$
TF	0.8390	0.2231	0.3525	0.1237	0.0511	0.1748	0.0238	11.1057	11.1057
TF+MLE	0.8130	0.9271	0.8662	0.0508	<b>0.0477</b>	0.0985	<b>0.0139</b>	1.4014	1.4016
TF+MLE+SFE	<b>0.9474</b>	<b>0.9419</b>	<b>0.9446</b>	<b>0.0431</b>	0.0531	<b>0.0962</b>	0.0142	<b>0.8988</b>	<b>0.8989</b>

Table 3: Ablation experiments on three model variations. TF: native Transformer; TF+MLE: TF with multi-level embedding module; TF+MLE+SFE: TF with multi-level embedding module and segment-based feature embeddings.

This makes the selection of the optimal parameter value easier for the user. Thus, DeepMerge overcomes scale selection, unlike other multi-scale segmentation methods. A closer-to-zero scale parameter denotes a high similarity while values close or greater than one, denote a low similarity. As shown in Fig.14, most feature spatial distances are clustered lower than 0.3 and higher than 0.9, showing a U-shaped distribution. Such a high degree of feature separation lays the foundation for the accurate segmentation of DeepMerge. Segment pairs with a feature distance smaller than 0.3 can be merged with a high probability. Segment pairs with a feature distance greater than 0.9 are very likely to be different geo-objects. The remaining problem is how to distinguish segment pairs in the middle range, into which where most optimal scales might fall. From Fig.12, we notice that segmented results in the scale range of  $[0.4, 0.7]$  are desirable for many applications, and the proposed DeepMerge is able to generate segmentation results in different scales as needed.

To ensure the efficiency of the merging process, many region-merging methods introduce the object size as a parameter in the merging criteria. Although such a strategy improves the merging efficiency and generates even-sized geo-objects, it fails to meet the demand of many applications due to the uneven size distribution of geo-objects in an image. For example, the tiny geo-objects in our dataset include individual trees and three-pixel wide intermittent sidewalks. In comparison, factory buildings and roads usually contain thousands of pixels as shown in Fig.15. The blue mask in the figure is the road segmented as a whole geo-object with  $166,981 \text{ m}^2$  in size. The polygons in the green box are four independent residential houses with an average area of  $1,000 \text{ m}^2$ . In the red box, there are three individual lawns, in which the smallest are of lawns only covers  $42 \text{ m}^2$ . In this case, the blue road area is 3,976 times the size of the smaller lawn. In this study, the segmentation results of DeepMerge are able to capture the true sizes of geo-objects.

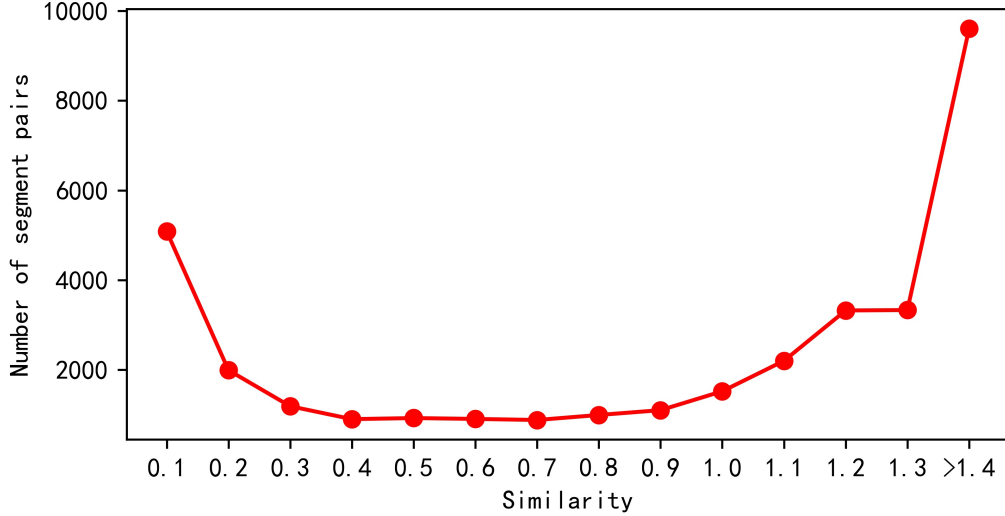


Figure 14: The feature spatial distance histogram given different scale parameters.

In other cases, the sizes of some geo-objects are difficult to measure when they lie across multiple images, such as continuous roads and vast green spaces. The proposed DeepMerge aims to maintain the true sizes of geo-objects, leading to uneven-sized segmentation results. We believe this property of the proposed DeepMerge is beneficial to many subsequent image analysis (e.g., GeOBIA). In particular, geo-objects are very likely to be separated across multiple images (Fig.13).

## 6. Conclusion

In this study, we proposed a deep learning-based region-merging method for multiscale segmentation of large-area and high-resolution remote sensing imagery. Given an initial primitive segmentation result, DeepMerge automatically obtains optimal segmentation output as vector format in an interpretable scale parameter.

Our method combines deep learning and region-merging. We introduced the multi-level embedding module into vision Transformer networks to capture the local and global information. In addition, we introduced the segment-based feature embedding module into the networks to hold the object features. The segmentation performance on the Phoenix city cluster of our proposed method performs out SOTA methods in both qualitative and quan-

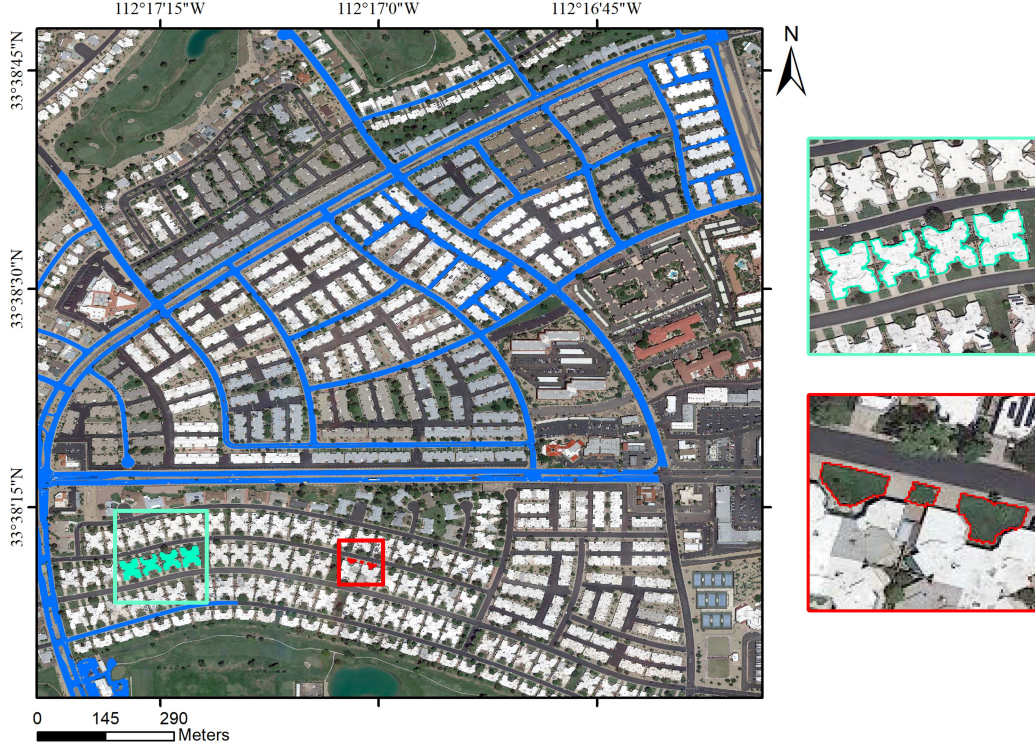


Figure 15: A case of geo-objects with various sizes for presentation.

titative measurements. The proposed method requires a small number of training samples with respect to the total number of segments. In our experimental analysis, only 0.19% of the total number of segments were labelled. DeepMerge based on a low ratio training dataset achieves high advancements of 0.1 in  $F$  value, large decrease of 0.04 in  $TE$ , and large decrease of 0.44 in  $ED2$  against SOTA methods. The optimal scale parameter of the proposed method stabilizes between 0.4 and 0.7 in different landscapes. This makes the selection of the optimal parameter value easier for the user. The proposed DeepMerge is suitable for the precise segmentation of large-area and very high-spatial-resolution remote sensing images. It will provide efficient and precise segmentation of products. However, it still requires training samples, leading to high time-consuming for segmentation in small areas.

We plan to direct our further works to the potential improvement and the wide applications of the proposed DeepMerge by exploring the possibility of developing unsupervised DeepMerge-based segmentation approaches and fur-

ther evaluating DeepMerge’s performance on various land-cover classification problems.

## 7. Acknowledgements

This work was supported by China Scholarship Council.

## References

- [1] X. Lv, Z. Shao, D. Ming, C. Diao, K. Zhou, C. Tong, Improved object-based convolutional neural network (iocnn) to classify very high-resolution remote sensing images, *International Journal of Remote Sensing* 42 (2021) 8318–8344.
- [2] W. Zhou, D. Ming, X. Lv, K. Zhou, H. Bao, Z. Hong, So-cnn based urban functional zone fine division with vhr remote sensing image, *Remote Sensing of Environment* 236 (2020) 111458.
- [3] C. N. Mundia, M. Aniya, Analysis of land use/cover changes and urban expansion of nairobi city using remote sensing and gis, *International journal of Remote sensing* 26 (2005) 2831–2849.
- [4] W. Zhao, C. Persello, A. Stein, Building outline delineation: From aerial images to polygons with an improved end-to-end learning framework, *ISPRS journal of photogrammetry and remote sensing* 175 (2021) 119–131.
- [5] J. Na, H. Ding, W. Zhao, K. Liu, G. Tang, N. Pfeifer, Object-based large-scale terrain classification combined with segmentation optimization and terrain features: A case study in china, *Transactions in GIS* 25 (2021) 2939–2962.
- [6] D. Chen, Y. Zhong, Z. Zheng, A. Ma, X. Lu, Urban road mapping based on an end-to-end road vectorization mapping network framework, *ISPRS Journal of Photogrammetry and Remote Sensing* 178 (2021) 345–365.
- [7] W. Zhao, C. Persello, A. Stein, Extracting planar roof structures from very high resolution images using graph neural networks, *ISPRS Journal of Photogrammetry and Remote Sensing* 187 (2022) 34–45.

- [8] T. Blaschke, Object based image analysis for remote sensing, *ISPRS journal of photogrammetry and remote sensing* 65 (2010) 2–16.
- [9] X. Zhang, P. Xiao, X. Feng, Fast hierarchical segmentation of high-resolution remote sensing image with adaptive edge penalty, *Photogrammetric Engineering & Remote Sensing* 80 (2014) 71–80.
- [10] K. Haris, S. N. Efstratiadis, N. Maglaveras, A. K. Katsaggelos, Hybrid image segmentation using watersheds and fast region merging, *IEEE Transactions on image processing* 7 (1998) 1684–1699.
- [11] X. Zhang, P. Xiao, X. Song, J. She, Boundary-constrained multi-scale segmentation method for remote sensing images, *ISPRS Journal of Photogrammetry and Remote Sensing* 78 (2013) 15–25.
- [12] J. Yang, Y. He, J. Caspersen, Region merging using local spectral angle thresholds: A more accurate method for hybrid segmentation of remote sensing images, *Remote sensing of environment* 190 (2017) 137–148.
- [13] R. Achanta, A. Shaji, K. Smith, A. Lucchi, P. Fua, S. Süsstrunk, Slc superpixels compared to state-of-the-art superpixel methods, *IEEE transactions on pattern analysis and machine intelligence* 34 (2012) 2274–2282.
- [14] M. V. d. Bergh, X. Boix, G. Roig, B. d. Capitani, L. V. Gool, Seeds: Superpixels extracted via energy-driven sampling, in: *European conference on computer vision*, Springer, 2012, pp. 13–26.
- [15] S. Paris, F. Durand, A topological approach to hierarchical segmentation using mean shift, in: *2007 IEEE Conference on Computer Vision and Pattern Recognition*, IEEE, 2007, pp. 1–8.
- [16] M. Baatz, Multi resolution segmentation: an optimum approach for high quality multi scale image segmentation, in: *Beutrage zum AGIT-Symposium*. Salzburg, Heidelberg, 2000, 2000, pp. 12–23.
- [17] D. R. Martin, C. C. Fowlkes, J. Malik, Learning to detect natural image boundaries using local brightness, color, and texture cues, *IEEE transactions on pattern analysis and machine intelligence* 26 (2004) 530–549.

- [18] P. Arbelaez, M. Maire, C. Fowlkes, J. Malik, Contour detection and hierarchical image segmentation, *IEEE transactions on pattern analysis and machine intelligence* 33 (2010) 898–916.
- [19] J. Pont-Tuset, P. Arbelaez, J. T. Barron, F. Marques, J. Malik, Multiscale combinatorial grouping for image segmentation and object proposal generation, *IEEE transactions on pattern analysis and machine intelligence* 39 (2016) 128–140.
- [20] C. Zhang, I. Sargent, X. Pan, H. Li, A. Gardiner, J. Hare, P. M. Atkinson, An object-based convolutional neural network (ocnn) for urban land use classification, *Remote sensing of environment* 216 (2018) 57–70.
- [21] L. Drăguț, O. Csillik, C. Eisank, D. Tiede, Automated parameterisation for multi-scale image segmentation on multiple layers, *ISPRS Journal of photogrammetry and Remote Sensing* 88 (2014) 119–127.
- [22] D. Ming, J. Li, J. Wang, M. Zhang, Scale parameter selection by spatial statistics for geobia: Using mean-shift based multi-scale segmentation as an example, *ISPRS Journal of Photogrammetry and Remote Sensing* 106 (2015) 28–41.
- [23] Z. Hu, Q. Zhang, Q. Zou, Q. Li, G. Wu, Stepwise evolution analysis of the region-merging segmentation for scale parameterization, *IEEE Journal of Selected Topics in Applied Earth Observations and Remote Sensing* 11 (2018) 2461–2472.
- [24] X. Zhang, P. Xiao, X. Feng, J. Wang, Z. Wang, Hybrid region merging method for segmentation of high-resolution remote sensing images, *ISPRS Journal of Photogrammetry and Remote Sensing* 98 (2014) 19–28.
- [25] Y. Shen, J. Chen, L. Xiao, D. Pan, Optimizing multiscale segmentation with local spectral heterogeneity measure for high resolution remote sensing images, *ISPRS Journal of Photogrammetry and Remote Sensing* 157 (2019) 13–25.
- [26] X. Zhang, P. Xiao, X. Feng, Object-specific optimization of hierarchical multiscale segmentations for high-spatial resolution remote sensing images, *ISPRS Journal of Photogrammetry and Remote Sensing* 159 (2020) 308–321.

- [27] S. Derivaux, S. Lefevre, C. Wemmert, J. Korczak, Watershed segmentation of remotely sensed images based on a supervised fuzzy pixel classification, in: 2006 IEEE International Symposium on Geoscience and Remote Sensing, IEEE, 2006, pp. 3712–3715.
- [28] J. Wassenberg, W. Middelmann, P. Sanders, An efficient parallel algorithm for graph-based image segmentation, in: International Conference on Computer Analysis of Images and Patterns, Springer, 2009, pp. 1003–1010.
- [29] B. Johnson, Z. Xie, Unsupervised image segmentation evaluation and refinement using a multi-scale approach, *ISPRS Journal of Photogrammetry and Remote Sensing* 66 (2011) 473–483.
- [30] H.-C. Lee, D. R. Cok, Detecting boundaries in a vector field, *IEEE Transactions on Signal Processing* 39 (1991) 1181–1194.
- [31] T. Su, T. Liu, S. Zhang, Z. Qu, R. Li, Machine learning-assisted region merging for remote sensing image segmentation, *ISPRS Journal of Photogrammetry and Remote Sensing* 168 (2020) 89–123.
- [32] J. Chen, M. Deng, X. Mei, T. Chen, Q. Shao, L. Hong, Optimal segmentation of a high-resolution remote-sensing image guided by area and boundary, *International Journal of Remote Sensing* 35 (2014) 6914–6939.
- [33] Y. Wang, Q. Qi, Y. Liu, L. Jiang, J. Wang, Unsupervised segmentation parameter selection using the local spatial statistics for remote sensing image segmentation, *International Journal of Applied Earth Observation and Geoinformation* 81 (2019) 98–109.
- [34] Z. Zheng, S. Du, S. Du, X. Zhang, A multiscale approach to delineate dune-field landscape patches, *Remote Sensing of Environment* 237 (2020) 111591.
- [35] A. Arnab, M. Dehghani, G. Heigold, C. Sun, M. Lučić, C. Schmid, Vivit: A video vision transformer, in: Proceedings of the IEEE/CVF International Conference on Computer Vision, 2021, pp. 6836–6846.



- [36] S. Chopra, R. Hadsell, Y. LeCun, Learning a similarity metric discriminatively, with application to face verification, in: 2005 IEEE Computer Society Conference on Computer Vision and Pattern Recognition (CVPR'05), volume 1, IEEE, 2005, pp. 539–546.
- [37] Q. Guo, W. Feng, C. Zhou, R. Huang, L. Wan, S. Wang, Learning dynamic siamese network for visual object tracking, in: Proceedings of the IEEE international conference on computer vision, 2017, pp. 1763–1771.
- [38] X. Lv, D. Ming, T. Lu, K. Zhou, M. Wang, H. Bao, A new method for region-based majority voting cnns for very high resolution image classification, *Remote Sensing* 10 (2018) 1946.
- [39] X. Lv, D. Ming, Y. Chen, M. Wang, Very high resolution remote sensing image classification with seeds-cnn and scale effect analysis for super-pixel cnn classification, *International Journal of Remote Sensing* 40 (2019) 506–531.
- [40] X. Lv, Z. Shao, X. Huang, W. Zhou, D. Ming, J. Wang, C. Tong, Bts: a binary tree sampling strategy for object identification based on deep learning, *International journal of geographical information science* 36 (2022) 822–848.
- [41] D. Hendrycks, K. Gimpel, Gaussian error linear units (gelus), *arXiv preprint arXiv:1606.08415* (2016).
- [42] X. Zhang, X. Feng, P. Xiao, G. He, L. Zhu, Segmentation quality evaluation using region-based precision and recall measures for remote sensing images, *ISPRS Journal of Photogrammetry and Remote Sensing* 102 (2015) 73–84.
- [43] T. Su, S. Zhang, Local and global evaluation for remote sensing image segmentation, *ISPRS Journal of Photogrammetry and Remote Sensing* 130 (2017) 256–276.
- [44] Y. Liu, L. Bian, Y. Meng, H. Wang, S. Zhang, Y. Yang, X. Shao, B. Wang, Discrepancy measures for selecting optimal combination of parameter values in object-based image analysis, *ISPRS journal of photogrammetry and remote sensing* 68 (2012) 144–156.

- [45] L. Yu, P. Gong, Google earth as a virtual globe tool for earth science applications at the global scale: progress and perspectives, *International Journal of Remote Sensing* 33 (2012) 3966–3986.
- [46] B. Chen, F. Qiu, B. Wu, H. Du, Image segmentation based on constrained spectral variance difference and edge penalty, *Remote Sensing* 7 (2015) 5980–6004.
- [47] Z. Hu, Q. Li, Q. Zhang, Q. Zou, Z. Wu, Unsupervised simplification of image hierarchies via evolution analysis in scale-sets framework, *IEEE Transactions on Image Processing* 26 (2017) 2394–2407.
- [48] N. Wang, F. Chen, B. Yu, Y. Qin, Segmentation of large-scale remotely sensed images on a spark platform: A strategy for handling massive image tiles with the mapreduce model, *ISPRS journal of photogrammetry and remote sensing* 162 (2020) 137–147.